

Robust Task-Specific Beamforming with Low-Resolution ADCs for Power-Efficient Hybrid MIMO Receivers

Eyyup Tasci, Timur Zirtiloglu, Alperen Yasar, Yonina C. Eldar, Nir Shlezinger, and Rabia Tugce Yazicigil

Abstract—Multiple-input multiple-output (MIMO) systems exploit spatial diversity to facilitate multi-user communications with high spectral efficiency by beamforming. As MIMO systems utilize multiple antennas and radio frequency (RF) chains, they are typically costly to implement and consume high power. A common method to reduce the cost of MIMO receivers is utilizing less RF chains than antennas by employing hybrid analog/digital beamforming (HBF). However, the added analog circuitry involves active components whose consumed power may surpass that saved in RF chain reduction. An additional method to realize power-efficient MIMO systems is to use low-resolution analog-to-digital converters (ADCs), which typically compromises signal recovery accuracy. In this work, we propose a power-efficient hybrid MIMO receiver with low-quantization rate ADCs, by jointly optimizing the analog and digital processing in a hardware-oriented manner using task-specific quantization techniques. To mitigate power consumption on the analog front-end, we utilize efficient analog hardware architecture comprised of sparse low-resolution vector modulators, while accounting for their properties in design to maintain recovery accuracy and mitigate interferers in congested environments. To account for common mismatches induced by non-ideal hardware and inaccurate channel state information, we propose a robust mismatch aware design. Supported by numerical simulations and power analysis, our power-efficient MIMO receiver achieves comparable signal recovery performance to power-hungry fully-digital MIMO receivers using high-resolution ADCs. Furthermore, our receiver outperforms the task-agnostic HBF receivers with low-rate ADCs in recovery accuracy at lower power and successfully copes with hardware mismatches.

I. INTRODUCTION

Multiple-input multiple-output (MIMO) technology is widely used in modern wireless communication systems due to their superior data capacity, improved coverage, and highly robust multi-user support [2]–[4]. Although the theoretical advantages of MIMO communications are well-established, practical trade-offs between power consumption, spectral efficiency, and reliability emerge in hardware implementations [5]–[7]. MIMO receivers utilize multiple signal acquisition chains for spatial signal processing, each consisting of a radio-frequency (RF) front end performing RF signal amplification with low noise, followed by down-conversion to baseband. These continuous-time analog baseband signals are translated

into a digital representation for further processing. Analog-to-digital conversion is performed in two steps: the continuous-time analog signal is sampled into a discrete-time signal, and then quantized into a discrete-amplitude representation stored as digital bits [8]. This process is usually carried out in hardware using uniform scalar analog-to-digital converters (ADCs) [9]. MIMO systems traditionally apply fully-digital data acquisition with spatial signal processing using high-resolution quantization and Nyquist sampling rates, leading to high power consumption and hardware design complexity.

A common approach to mitigate the increased cost of MIMO receivers is to utilize fewer RF chains and ADCs than antennas via hybrid analog/digital beamforming (HBF). Such architectures incorporate an additional analog combiner circuit before the acquisition, allowing dimensionality reduction [10], [11] while preserving the ability of the MIMO array in achieving directed beamforming via, e.g., holographic techniques [12]. In fact, HBF is also utilized without RF chain reduction to boost pre-acquisition spatial interferer rejection [13]–[16]. Nonetheless, the introduction of an analog combiner comprised of active components may also be power-hungry. An additional power reduction technique is to use low-resolution acquisition, connecting each antenna to a low-quantization rate ADC [17]–[20]. However, the distortion added by coarse quantization results in degraded signal recovery.

Recently, a task-specific quantization framework was introduced to design MIMO receivers that combine both HBF with bit-constrained ADCs [21]–[24]. In task-specific quantization, the analog front end is designed to be aware of the use of low-resolution ADCs and the desired task. Task-specific receivers combine the signals in analog such that the quantization distortion hardly affects the task information recovered in digital. Task-specific design yield improved signal recovery in MIMO communications [7], [25], [26] and radar [27].

Despite its performance gains, implementing MIMO receivers utilizing task-specific quantization gives rise to challenges associated with the usage of a configurable analog combiner. First, such circuitry may rely on costly and power-hungry active components. Moreover, the task-specific design configures the analog front end based on the channel state information, e.g., knowledge of the angle-of-arrivals (AoAs) of the desired signals. While this assumption is often adopted in adaptive beamforming systems [13]–[16], [28], it makes the system sensitive to AoA inaccuracies. Current literature on tackling such mismatches via robust adaptive beamforming, e.g., [28], assumes usage of infinite-resolution ADCs, and has not been employed in low-bit settings. Furthermore, in practice, analog circuitry, and particularly limited cost and

Parts of this work were presented in the 2022 IEEE International Conference on Acoustics, Speech, and Signal Processing (ICASSP) as the paper [1]. E. Tasci, T. Zirtiloglu, A. Yasar, and R. T. Yazicigil are with the Department of ECE, Boston University, Boston, MA (e-mail: {etasci2, timurz, ayasar, rty}@bu.edu). N. Shlezinger is with the School of ECE, Ben-Gurion University of the Negev, Beer-Sheva, Israel (e-mail: nirshl@bgu.ac.il). Y. C. Eldar is with the Faculty of Math and CS, Weizmann Institute of Science, Rehovot, Israel (e-mail: yonina.eldar@weizmann.ac.il). E. Tasci and T. Zirtiloglu contributed equally to this work.

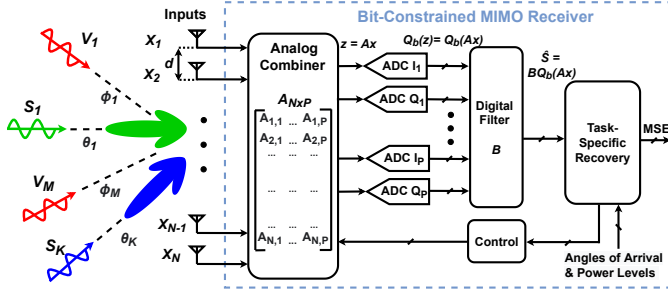


Fig. 1. Task-specific hybrid MIMO receiver system.

configurable designs, induce mismatches, such that the gain and phase response of the analog combiner may differ from the ideal response. Such mismatches degrade task recovery performance of the system [29], [30]. The above challenges motivate a hardware-aware design of low-bit HBF receivers, which accounts for low-power and non-ideal combiner circuitry while coping with AoA mismatches.

In this work, we study power-efficient hybrid MIMO receivers implementing bit-constrained signal recovery under AoA mismatches and hardware non-idealities. We consider MIMO communications in congested environments, where the system task is to recover the desired signals and reject interferers. We present a hardware architecture utilizing low-resolution ADCs and a programmable analog pre-processing front end. Since power consumption is highly implementation-dependent, we consider analog combiners implemented using vector modulators (VMs), which is a common circuitry for realizing configurable gain and phase [31]. Since the analog power consumption is directly proportional to the hardware complexity [32], we reduce the power by boosting the VMs to be either discrete or sparsely activated [1]. We propose a task-specific algorithm co-integrating these hardware-level techniques for accurate and power-efficient signal recovery.

Next, we propose a robust counterpart of the task-specific design that co-optimizes power-efficient recovery in the presence of mismatches. We tackle the presence of AoA errors by proposing a robust HBF design and cope with hardware non-idealities by developing a hardware-compliant model, which is incorporated into the design procedure. We compare the proposed system with task-agnostic MIMO systems in terms of signal recovery accuracy, receiver beam pattern, and power consumption. For the latter, we use power profiles derived from the measured power consumption of state-of-the-art hardware implementations [10], [14], [33]–[37]. Our comparative study shows that at a significantly reduced quantization rate, our design achieves accurate signal recovery comparable to the performance of fully-digital MIMO receivers using high-resolution ADCs while being robust to practical mismatches. Furthermore, the task-specific receiver notably outperforms task-agnostic architectures operating under similar bit constraints. Regarding beam pattern, we demonstrate that our design attenuates the interferers by ≥ 30 dB while still being able to provide sufficient gain for desired signals. The task-specific receiver reduces the power consumption by at least 58% compared to task-agnostic fully-digital MIMO and HBF receivers.

The rest of the paper is organized as follows: Section II reviews the system model and presents the receiver architecture. The non-mismatched HBF design algorithm is provided in Section III, and its robust counterpart is derived in Section IV. Section V analyzes our model-based performance evaluation supported by numerical simulations and power consumption estimates, and Section VI concludes the paper.

Throughout the paper, we use boldface lower-case letters for vectors and boldface upper-case letters for matrices. The n th element of a vector \mathbf{x} and the (n, m) th element of a matrix \mathbf{X} are denoted as $[x]_n$ and $[\mathbf{X}]_{n,m}$, respectively. We use j , $(\cdot)^H$, $\mathbb{E}\{\cdot\}$, $\text{Re}\{\cdot\}$, and $\text{Im}\{\cdot\}$ for the imaginary unit, Hermitian transpose, stochastic expectation, real and imaginary parts. Finally, \mathbf{I}_n is the $n \times n$ identity matrix, and \mathbb{C} is the set of complex numbers.

II. SYSTEM MODEL

In the following, we first review the signal model relating the observed signals and the task vector, hardware implementation of our design, and possible system mismatches in Subsection II-A. Then, based on these models, we formulate the system design problem in Subsection II-B.

A. Hybrid MIMO Receiver with Embedded Beamforming

We study low-power hybrid MIMO receivers, focusing on the task of recovering desired signals under the presence of interferers via beamforming. Our description of the system operation commences with the received signals, after which we model the operations of the ADCs, analog pre-processing, and common non-idealities that are likely to be encountered in such settings.

1) *Signal Model*: Consider a hybrid MIMO receiver with N antenna elements and P RF chains. Two ADCs are needed in each RF chain to quantize down converted in- (I) and quadrature-phase (Q) baseband signals, resulting in $2 \cdot P$ ADCs in total. All signals are assumed to be sampled above Nyquist sampling rate, yet the ADCs have finite rate quantizers. Let $\mathbf{x} = [x_1, \dots, x_N]$ be the vector signal observed at the N antenna elements. The received signal \mathbf{x} incorporates a set of K desired signals denoted $[s_1, \dots, s_K]$, received from sources at relative angles $[\theta_1, \dots, \theta_K]$, respectively. The received signal also includes M interferers denoted $[v_1, \dots, v_M]$, from sources at relative angles $[\phi_1, \dots, \phi_M]$, respectively. We assume that the receiver has the prior knowledge of AoAs of desired signals and interferers. All sources are assumed to be narrowband Gaussian signals lying at the far-field, and thus the received signal is

$$\mathbf{x} = \sum_{k=1}^K s_k \mathbf{a}(\theta_k) + \sum_{m=1}^M v_m \mathbf{a}(\phi_m) + \mathbf{w}. \quad (1)$$

In (1), \mathbf{w} is additive white Gaussian noise with variance σ_w^2 , and $\mathbf{a}(\psi) \in \mathbb{C}^N$ is the steering vector whose entries are

$$[\mathbf{a}(\psi)]_n = e^{-j2\pi n \frac{d}{\lambda} \sin \psi}, \quad (2)$$

where d is the spacing between antenna elements and λ is the wavelength of the received signals. An illustration of this system is depicted in Fig. 1.

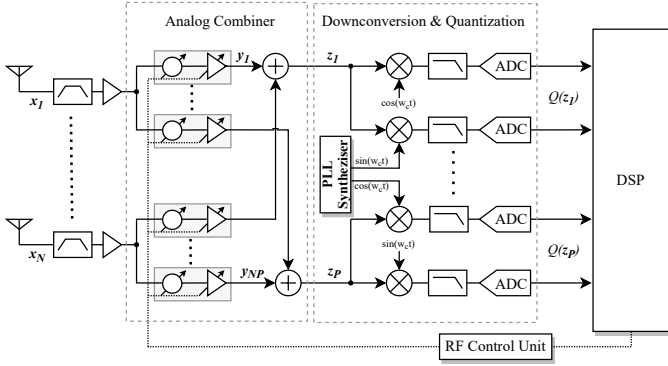


Fig. 2. Schematic of a hybrid MIMO hardware implementation.

Define the steering matrices $M_\theta \in \mathbb{C}^{N \times K}$ and $M_\phi \in \mathbb{C}^{N \times M}$ such that $[M_\theta]_{n,k} = [\mathbf{a}(\theta_k)]_n$ and $[M_\phi]_{n,m} = [\mathbf{a}(\phi_m)]_n$, and let $\mathbf{s} = [s_1, \dots, s_N]$ and $\mathbf{v} = [v_1, \dots, s_M]$ be the desired signal and interferer vectors, respectively. We can then write (1) as

$$\mathbf{x} = M_\theta \mathbf{s} + M_\phi \mathbf{v} + \mathbf{w}. \quad (3)$$

By letting C_s and C_v be the covariance matrices of \mathbf{s} and \mathbf{v} , respectively, it follows from (3) that the covariance matrix of the received signal \mathbf{x} is

$$C_x = M_\theta C_s M_\theta^H + M_\phi C_v M_\phi^H + \sigma_w^2 I_N, \quad (4a)$$

and its correlation with the task of interest \mathbf{s} is given by

$$C_{s\mathbf{x}} = C_s M_\theta^H. \quad (4b)$$

2) *Signal Acquisition*: We focus on hybrid MIMO receivers operating with low-resolution ADCs. Here, the acquisition of \mathbf{x} includes pre-processing in the analog domain followed by its down-conversion and quantization into digital form.

Let $\mathbf{A} \in \mathbb{C}^{P \times N}$ be the analog combiner matrix that performs analog pre-processing. The observed signal is processed in analog first, generating the $P \times 1$ representation of the analog combiner output $\mathbf{z} = [z_1, \dots, z_P]$, which is forwarded to the ADCs. Hence, the output vector \mathbf{z} is given by

$$\mathbf{z} = \mathbf{A}\mathbf{x}. \quad (5)$$

The acquisition thus includes the conversion of \mathbf{z} into digital by the ADCs, and the setting of the analog combiner \mathbf{A} .

Analog Hardware: A high level hardware architecture implementing a hybrid MIMO system is depicted in Fig. 2. The analog combiner \mathbf{A} represents the adjustable analog pre-processing carried out on the received signals prior to their conversion to digital. The complex multiplication that each element of \mathbf{A} performs can be realized by means of serial phase shifters and variable gain amplifiers (VGAs). Another alternative that is commonly used for implementing reconfigurable analog processing, which is considered in this work, utilizes VMs with low noise. Here, each complex entry of \mathbf{A} corresponds to a single VM component, thus, for the $N \times P$ analog combiner matrix \mathbf{A} , a total of $N \times P$ VMs are utilized. Signals are summed and downconverted at the output producing $2 \cdot P$ baseband output voltages, which are used as inputs to the ADCs.

VMs: A VM is an analog circuitry that applies different variable gain and polarization to each of the I/Q components of a signal to realize gain and phase shift. The mapping carried out by each VM is constrained to take values in a discrete set \mathcal{A} . To accommodate the ability to deactivate a VM, we assume that $0 \in \mathcal{A}$. The resulting model for a VM-based analog combiner, where the entries of \mathbf{A} take values in \mathcal{A} , accommodates various architectures, such as phase-shifter-based combiners [10], for which \mathcal{A} is the union of the unit circle and the origin.

Since such analog processing can be costly in terms of power, one often utilizes Cartesian VMs, known to be highly power efficient [38]. The building blocks of a Cartesian VM are illustrated in Fig. 3a. Here, the VM input is first converted to its differential parts by a balun. The differential input is then fed into a quadrature all-pass filter, yielding four orthogonal components with a phase shift of 0° , 180° , 90° , and 270° in its output. The quadrant of the final vector is determined by selecting the corresponding I/Q paths, while other unused paths are terminated with matched impedance. The desired complex gain can be realized by properly weighting the selected orthogonal components in magnitude using VGAs. The control signals of the VGAs are generated by the r -bit digital output of the digital-to-analog converter, which determines a discrete set \mathcal{A} and the resolution of the Cartesian VM. Higher resolution of complex gain/phase states comes at the cost of higher power consumption. The vectors generated at the output of each block are illustrated at the top of Fig. 3a. For the r -bit Cartesian VM architecture, the set \mathcal{A} is given as

$$\mathcal{A} = \left\{ g + jh \mid g, h \in \left\{ 0, \pm \frac{2}{2^r}, \pm \frac{4}{2^r}, \dots, \pm 1 \right\} \right\}. \quad (6)$$

Fig. 3b illustrates the normalized complex constellation of all available complex gain/phase states for a 4-bit VM.

ADCs: The analog combiner output \mathbf{z} is converted into a digital representation using $2 \cdot P$ identical uniform ADCs, each with b levels. The overall number of bits used for representing \mathbf{x} in digital is thus $2 \cdot P \lceil \log_2 b \rceil$. The resulting vector processed in the digital domain is $\mathcal{Q}_b(\mathbf{z})$, where $\mathcal{Q}_b(\cdot)$ is the element-wise uniform quantization operator with b levels.

3) *Common Non-Idealities*: Hybrid MIMO beamforming is often carried out under hardware and environmental non-idealities. In the following, we evaluate our system robustness under two types of mismatches: (1) inaccurate knowledge of the AoAs of the desired users; and (2) hardware non-idealities stemming from phase and gain errors in the VMs.

Inaccurate AoAs: A common mismatch encountered in MIMO beamforming occurs when the receiver has a noisy estimate of the true AoAs of the desired signals $\boldsymbol{\theta} = [\theta_1, \dots, \theta_K]$. This may arise due to the limited resolution of the AoA estimation sensors and localization errors. Moreover, a malicious adversary can attack a task-specific sensor by corrupting the estimated AoAs provided to the system. To incorporate such mismatches into our system model, we represent the AoAs $\boldsymbol{\theta}$ by a noisy estimate with an error margin. Assuming the mismatches of the AoAs are limited to some degree $\epsilon > 0$, we define an interval $\Theta(\boldsymbol{\theta}, \epsilon)$ that contains the true AoAs as:

$$\Theta(\boldsymbol{\theta}, \epsilon) = \{ \bar{\boldsymbol{\theta}} \mid \|\bar{\boldsymbol{\theta}} - \boldsymbol{\theta}\|_\infty \leq \epsilon \}. \quad (7)$$

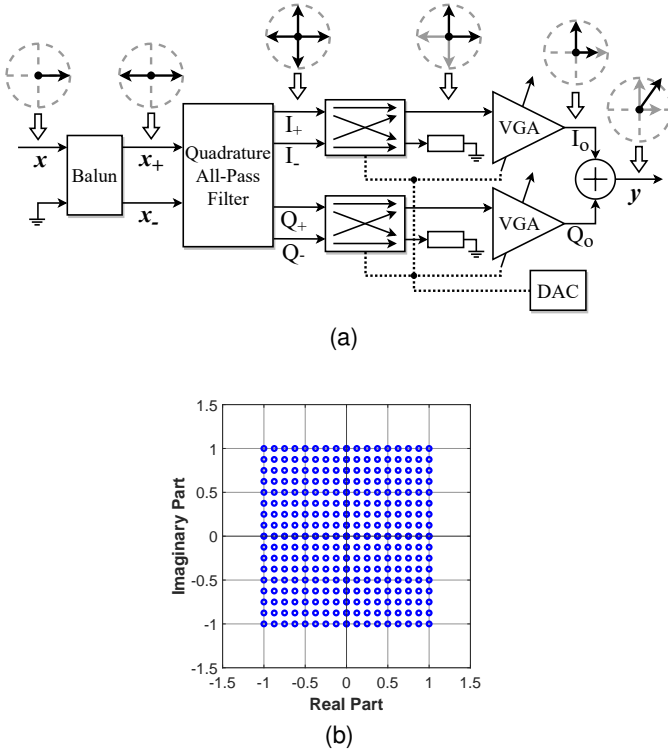


Fig. 3. (a) VM architecture and (b) constellation diagram of a 4-bit VM.

Phase/Gain Mismatches in the Analog Hardware: The analog pre-processing hardware has impairments in practice. In this work, we consider linear hardware impairments, including the phase and gain mismatches between the I/Q paths in VMs. Mismatches in the circuitry of quadrature all-pass filters or in VGAs in VMs typically results in imbalances in the amplitude and phase of the output of the analog pre-processing, i.e., in z . Such mismatches can occur within a single VM, as well as between different VMs, severely impacting the recovery accuracy if they are not calibrated. Under phase and gain mismatches, the matrix \mathbf{A} cannot perform accurate complex multiplication, hence the set \mathcal{A} becomes corrupted. We denote this corrupted set by $\bar{\mathcal{A}}$. Hardware-compliant mathematical modeling of $\bar{\mathcal{A}}$ is proposed in Section IV.

B. Problem Formulation

Our goal is to tune the analog combiner \mathbf{A} based on the above signal and hardware model. Our design is optimized for multiple tasks simultaneously, including accurate signal recovery, spatial interferer suppression, and power efficiency. We aim for the task-specific MIMO receiver to perform robust recovery when deployed under noisy estimation of the AoAs and hardware non-idealities.

Signal Recovery: The main task of the receiver is to recover the desired signal \mathbf{s} from the digital representation $\mathcal{Q}_b(z)$. Our design objective is the mean-squared error (MSE), being widely used for evaluating signal recovery, and is closely related to the error vector magnitude (EVM) measure utilized in evaluating acquisition hardware. The MSE is defined by

$$\text{MSE} := \mathbb{E}\{\|\mathbf{s} - \mathbb{E}\{\mathbf{s}|\mathcal{Q}_b(z)\}\|^2\}. \quad (8)$$

Interferer Suppression: The MSE objective focuses only on the ability to recover \mathbf{s} . As such, it may prefer settings of

\mathbf{A} in which the effect of \mathbf{v} is mitigated in digital. In practice, it is often preferable to reject interferers in the analog domain, since strong spatial interferers may lead to receiver desensitization and increased dynamic range requirement of the ADCs [39]. Consequently, we explicitly require the analog combiner to suppress the spatial interferers. Since the contribution of \mathbf{v} on the analog combiner output z takes the form $\mathbf{A}\mathbf{M}_\phi$, we penalize interferer rejection via the max norm of $\mathbf{A}\mathbf{M}_\phi$, i.e.,

$$\text{IntRej}(\mathbf{A}) := \|\mathbf{A}\mathbf{M}_\phi\|_{\max} = \max_{i,j} (|[\mathbf{A}\mathbf{M}_\phi]_{i,j}|). \quad (9)$$

Power Efficiency: The power consumption of the MIMO receiver front end is dictated by the individual cost of each hardware component, including local oscillator generators (LO Gen), low-noise amplifiers, mixers, filters, and ADCs. Under the commonly employed ADC performance measure Walden figure of merit (FOM) [9], $P_{\text{ADC}}/(f_s \cdot 2^{\text{ENOB}})$, the performance of the ADC becomes proportional to the power consumption P_{ADC} , inversely proportional to the sampling rate, f_s , and the effective number of bits (ENOB), which is approximately proportional to the number of levels b [40].

The power consumption of an analog combiner hardware \mathbf{A} is highly dependent on two factors: 1) how many different values can its entries take, i.e., $|\mathcal{A}|$. This quantity is dictated by the resolution of VMs; and 2) which of its entries are active, namely, the sparsity level of \mathbf{A} . If the sparsity level of \mathbf{A} increases while reducing its resolution, i.e., using a coarse \mathbf{A} , the receiver power consumption is significantly reduced.

Robustness to Mismatches: As we show in Section III, the MSE objective can be formulated as a function of the AoAs of the desired signals, which are assumed to be known up to some degree ϵ . However, tuning the system using an inaccurate estimation of the AoAs may lead to high recovery errors. To address this problem, the analog combiner matrix \mathbf{A} and the digital processing should be designed by incorporating the range of possible AoAs, $\Theta(\theta, \epsilon)$, into the MSE objective, where the maximal tolerable error ϵ is assumed to be known.

Under gain and phase imbalances due to hardware impairments, the analog combiner \mathbf{A} does not perform the ideal complex multiplication that it is tuned for. Instead, it performs a complex multiplication corresponding to one of the values in the corrupted discrete set $\bar{\mathcal{A}}$. We aim to make our system robust against these hardware mismatches by requiring that the elements of the analog combiner matrix \mathbf{A} can only be configured to the values of the set $\bar{\mathcal{A}}$.

III. NON-MISMATCHED LOW-POWER HBF

The HBF design problem detailed in Subsection II-B accounts for several practical considerations. We initially consider that the system operates without the hardware mismatches and inaccurate AoAs to tackle this challenging design problem gradually. Namely, our goal here is to propose a design scheme which jointly accounts for the requirements of signal recovery, power consumption, and analog interference rejection. We consider the case where the number of ADCs (P), their resolution (b), and the values that the VMs can be configured to (\mathcal{A}) are dictated by the hardware performance requirements, and optimize \mathbf{A} accordingly. In particular, we

first focus on signal recovery in Subsection III-A, then we incorporate interferer suppression and power reduction in Subsection III-B. The resulting design is summarized in Subsection III-C, and its properties are discussed in Subsection III-D.

A. Signal Recovery via Task-Specific Quantization

We formulate the recovery error of the desired signal \mathbf{s} from its estimate $\hat{\mathbf{s}} = \mathbb{E}\{\mathbf{s}|\mathcal{Q}_b(\mathbf{z})\}$. For any quantized representation of $\hat{\mathbf{s}}$, the orthogonality principle implies that (8) can be decomposed as

$$\text{MSE} = \mathbb{E}\{\|\mathbf{s} - \hat{\mathbf{s}}\|^2\} = \mathbb{E}\{\|\mathbf{s} - \tilde{\mathbf{s}}\|^2\} + \mathbb{E}\{\|\tilde{\mathbf{s}} - \hat{\mathbf{s}}\|^2\}, \quad (10)$$

where $\tilde{\mathbf{s}}$ is minimum MSE (MMSE) estimate of the desired signal \mathbf{s} (which is a linear estimate for the model in (1) since the sources are Gaussian). The recovery error in (10) is given by the sum of the MMSE and the distortion with respect to the MMSE estimate $\tilde{\mathbf{s}}$. The second term depends on the configuration of the analog pre-processing, whereas the first term does not. One can thus use the excess MSE with respect to $\tilde{\mathbf{s}}$, which depends on \mathbf{A} and is denoted henceforth as $\text{ExMSE}(\mathbf{A})$, as the signal recovery measure.

Configuring \mathbf{A} which minimizes (10) is a special case of the task-specific (task-based) quantization setup studied in [21]. There, it was shown that while minimizing (10) is likely to be analytically intractable, one can obtain accurate signal recovery by modeling the ADCs as implementing non-subtractive dithered quantization while aiming to recover the MMSE estimate of \mathbf{s} . By defining $\mathbf{\Gamma} \triangleq \mathbf{C}_{s\mathbf{x}}\mathbf{C}_{\mathbf{x}}^{-1}$, the MMSE estimate can be written as $\tilde{\mathbf{s}} = \mathbf{\Gamma}\mathbf{x}$. Since the MMSE estimate is linear, we let the digital processing outputs an estimate of the form $\hat{\mathbf{s}} = \mathbf{B}\mathcal{Q}_b(\mathbf{A}\mathbf{x})$ for some $\mathbf{B} \in \mathbb{C}^{K \times P}$. In [21], it is discussed that the choice of linear MMSE estimate does not affect the overall performance significantly because $\tilde{\mathbf{s}}$ is the linear MMSE estimate of the desired signal. This holds true especially when the quantization error is small.

To formulate the MSE objective under the above considerations, set $\kappa := \eta^2(1 - \frac{\eta^2}{3b^2})^{-1}$ where η is a coefficient tuned to guarantee negligible overloading probability of the ADCs by determining the ratio of the ADC dynamic range to the standard deviation of its input. For instance, by setting $\eta = 3$ one guarantees overloading with probability of at most 11% for arbitrary signals by Chebyshev's inequality, and of less than 1% for Gaussian signals. We can now reformulate the MSE in (10) as stated in the following lemma (adapting [21, Lem. 1] to complex signals):

Lemma 1. *When the ADCs utilize non-subtractive dithered quantizers with vanishing overloading probability, the excess MSE in the objective (10) becomes*

$$\begin{aligned} \text{ExMSE}(\mathbf{A}) = & \text{Tr} \left(\mathbf{\Gamma}\mathbf{C}_{\mathbf{x}}\mathbf{\Gamma}^H - \mathbf{\Gamma}\mathbf{C}_{\mathbf{x}}\mathbf{A}^H \left(\mathbf{A}\mathbf{C}_{\mathbf{x}}\mathbf{A}^H \right. \right. \\ & \left. \left. + \frac{2\kappa \cdot \text{Tr}(\mathbf{A}\mathbf{C}_{\mathbf{x}}\mathbf{A}^H)}{3b^2 \cdot P} \mathbf{I}_P \right)^{-1} \mathbf{A}\mathbf{C}_{\mathbf{x}}\mathbf{\Gamma}^H \right). \end{aligned} \quad (11)$$

This MSE is achieved by setting the digital filter to be

$$\mathbf{B}(\mathbf{A}) = \mathbf{\Gamma}\mathbf{C}_{\mathbf{x}}\mathbf{A}^H \left(\mathbf{A}\mathbf{C}_{\mathbf{x}}\mathbf{A}^H + \frac{2\kappa \cdot \text{Tr}(\mathbf{A}\mathbf{C}_{\mathbf{x}}\mathbf{A}^H)}{3b^2 \cdot P} \mathbf{I}_P \right)^{-1}. \quad (12)$$

The digital matrix \mathbf{B} in Lemma 1 is the linear MMSE estimation matrix given $\mathcal{Q}_b(\mathbf{A}\mathbf{x})$. While Lemma 1 rigorously holds under some limiting assumptions on the system operation, i.e., using non-subtractive dithered quantizers, it also approximately holds when these assumptions are not satisfied for a broad range of input signals [21]. In the following, we exploit this representation of the MSE objective to incorporate additional design considerations such that \mathbf{A} is optimized while meeting the performance requirements detailed in Subsection II-B.

B. Low-Power Interferer Suppression

The objective (10) admits a closed-form minimizer, see [21, Thm. 1]. However, such a design only considers the signal recovery task and does not impose any structure on \mathbf{A} . To account for the interference rejection requirement and to balance the power consumption of the analog circuitry, we formulate our design objective as

$$\mathcal{L}(\mathbf{A}) = \text{ExMSE}(\mathbf{A}) + \gamma_I \text{IntRej}(\mathbf{A}) + \gamma_S \|\mathbf{A}\|_{1,1}. \quad (13)$$

In (13), $\|\cdot\|_{1,1}$ is the entry-wise ℓ_1 norm operator, encouraging the design to deactivate multiple VMs. The usage of the ℓ_1 norm can be interpreted as a convex relaxation of explicitly imposing sparsity via ℓ_0 -minimization [41, Ch. 2]. The term $\text{IntRej}(\cdot)$ defined in (9) boosts the suppression of spatial interferers, and it is convex since it is defined via the maximum norm. Finally, the hyperparameters $\gamma_I, \gamma_S > 0$ are regularization coefficients, balancing the contribution of signal recovery MSE, spatial interferer rejection, and sparsity level of the analog combiner in the overall loss measure $\mathcal{L}(\mathbf{A})$.

The final consideration which is not accounted for in (13) is the usage of discretized VMs. The resulting optimization is

$$\mathbf{A}^\circ = \arg \min_{\mathbf{A} \in \mathcal{A}^{P \times N}} \mathcal{L}(\mathbf{A}). \quad (14)$$

The fact that the optimization problem is formulated over a discrete (i.e., non-convex) search space makes obtaining \mathbf{A} that optimizes the objective within \mathcal{A} extremely challenging. Nonetheless, one can utilize discrete optimization to recover suitable designs of \mathbf{A} , as proposed next.

C. Analog Combiner Design

Since the optimization problem (14) seeks to minimize its objective over a discrete set, we tackle it using projected gradient based optimization. Our design strategy is comprised of k_{\max} iterations for minimizing $\mathcal{L}(\mathbf{A})$ over $\mathbb{C}^{P \times N}$, with periodic projections onto the discrete \mathcal{A} . We use $\mathcal{O}_{\mathcal{L}}(\cdot)$ to denote the iterative optimizer with loss measure \mathcal{L} .

By dividing the loss (13) into a *task* term $\tilde{\mathcal{L}}(\mathbf{A}) := \text{ExMSE}(\mathbf{A}) + \gamma_I \text{IntRej}(\mathbf{A})$ (measuring signal recovery and interference rejection performance) and a *prior* term $\gamma_S \|\mathbf{A}\|_{1,1}$

(boosting sparsity of the analog combiner), a candidate iterative method is proximal gradient descent. Here, each iteration first computes a gradient step in $\tilde{\mathcal{L}}(\mathbf{A})$ with step-size $\mu > 0$, and then takes the proximal mapping with respect to $\gamma_S \|\mathbf{A}\|_{1,1}$. The resulting iterative procedure is [41, Ch. 3]:

$$\begin{aligned} \mathcal{O}_{\mathcal{L}}(\mathbf{A}) &= \arg \min_{\mathbf{A} \in \mathbb{C}^{P \times N}} \gamma_S \|\tilde{\mathbf{A}}\|_{1,1} + \frac{1}{2} \left\| \tilde{\mathbf{A}} - (\mathbf{A} - \mu \nabla_{\mathbf{A}} \tilde{\mathcal{L}}(\mathbf{A})) \right\|_{2,2}^2 \\ &= \mathcal{T}_{\gamma_S} \{ \mathbf{A} - \mu \nabla_{\mathbf{A}} (\text{ExMSE}(\mathbf{A}) + \gamma_I \text{IntRej}(\mathbf{A})) \}. \end{aligned} \quad (15)$$

Here, \mathcal{T} is the element-wise complex soft-thresholding operator, given by $\mathcal{T}_{\lambda}(z) := e^{j \arg(z)} \max(|z| - \lambda, 0)$. Note that both the MSE in (11) and the interference rejection penalty in (9) are differentiable in \mathbf{A} , and the gradient can be computed using automatic differentiation engines, e.g., Autograd [42].

Every k_{proj} iterations, the intermediate $\mathbf{A}^{(k)}$ is projected to account for the discrete VMs via the element-wise projection operator $\mathcal{P}_{\mathcal{A}}(z) := \arg \min_{a \in \mathcal{A}} \|a - z\|_2$. In particular, for the r -bit Cartesian VM architecture, the projection operator boils down to element-wise uniform quantization, namely,

$$[\mathcal{P}_{\mathcal{A}}(\mathbf{A})]_{p,n} = \mathcal{Q}_{2^{r+1}} \left([\text{Re}\{\mathbf{A}\}]_{p,n} \right) + j \mathcal{Q}_{2^{r+1}} \left([\text{Im}\{\mathbf{A}\}]_{p,n} \right), \quad (16)$$

with $\mathcal{Q}_b(\cdot)$ being the b level uniform mid-tread quantizer (see Subsection II-A). The resulting algorithm is summarized as Algorithm 1. The hyperparameters of Algorithm 1 are the regularization coefficients γ_I, γ_S , the iteration limits $k_{\text{max}}, k_{\text{proj}}$, and the initial setting of $\mathbf{A}^{(0)}$. These add up to the individual hyperparameters of the optimizer $\mathcal{O}_{\mathcal{L}}(\cdot)$. In our experimental study, where the number of complex ADCs is equal to the number of desired sources, i.e., $P = K$, we use $\mathbf{A}^{(0)} = \mathbf{\Gamma}$ as our initial estimate, and set the digital filter \mathbf{B} via (12).

Algorithm 1: Analog Combiner Setting

Init: Fix $\mathbf{A}^{(0)}$
1 for $k = 1, 2, \dots, k_{\text{max}}$ **do**
2 Update $\mathbf{A}^{(k)} \leftarrow \mathcal{O}_{\mathcal{L}}(\mathbf{A}^{(k-1)})$ (see (15))
3 **if** $\text{mod}(k, k_{\text{proj}}) = 0$ **then**
4 Project via $\mathbf{A}^{(k)} \leftarrow \mathcal{P}_{\mathcal{A}}(\mathbf{A}^{(k)})$ (see (16))
5 **end**
6 end
Output: Analog combiner $\mathbf{A}^{(k_{\text{max}})}$.

D. Discussion

Algorithm 1 allows tuning of the hybrid MIMO receiver to accurately carry out signal recovery and interferer rejection simultaneously while boosting low-power implementation. Although we do not directly optimize the power consumption, efficiency naturally follows from the usage of sparse discrete VMs and few-bit ADCs. In fact, in Section V, we show that by utilizing Algorithm 1 to design a task-specific hybrid beamformer with low-resolution ADCs and quantized VMs with sparsity, one can achieve comparable or improved MSE compared to task-agnostic hybrid receivers while consuming half the power at a 4× reduced quantization rate.

The ability to configure hybrid beamformers in a manner that is simultaneously task- and energy-aware gives rise to several challenges. The first is the fact that Algorithm 1 assumes accurate knowledge of the AoAs and fully-calibrated analog hardware. As in practice, one is likely to cope with mismatches, as discussed in Subsection II-B, the design has to be extended to be robust to such inaccuracies. An additional challenge stems from the dynamic nature of wireless MIMO receivers, which implies that one should frequently reconfigure its hardware, particularly when the signal sources are mobile wireless users. The operation of Algorithm 1, which involves multiple iterations, can thus be too lengthy to be repeatedly utilized in real-time. A possible way to allow the design algorithm to be carried out efficiently with a small and fixed number of iterations is by leveraging data via deep unfolding methodology [43], [44]. We leave this for future investigation.

Algorithm 1 assumes that the number of ADCs (P) and their resolution (b) are given. Indeed, these parameters are typically fixed for a given device and are thus not considered in the optimization procedure. However, one can utilize the proposed algorithmic steps to optimize the number of bits and the number of ADCs, as done in, e.g., [22]. This can be beneficial when designing the hardware prior to its fabrication, or when employing ADCs with programmable resolutions.

IV. ROBUST LOW-POWER HBF

In this section, we re-design our system to be robust to mismatches, as stated in Subsection II-B. We extend Algorithm 1 and make it robust to inaccurate AoAs in Subsection IV-A, and to hardware non-idealities in Subsection IV-B. The resulting system operation is then discussed in Subsection IV-C.

A. Inaccurate AoAs

The proposed tuning of the analog combiner requires prior knowledge of the AoAs and power levels. These are used to form the correlation matrices $\mathbf{C}_{\mathbf{x}} = \mathbf{M}_{\theta} \mathbf{C}_{\mathbf{s}} \mathbf{M}_{\theta}^H + \mathbf{M}_{\phi} \mathbf{C}_{\mathbf{v}} \mathbf{M}_{\phi}^H + \sigma_w^2 \mathbf{I}_N$, and $\mathbf{C}_{\mathbf{s}\mathbf{x}} = \mathbf{C}_{\mathbf{s}} \mathbf{M}_{\theta}^H$. This information should therefore be either estimated or externally provided by a spatial sensor and may thus contain errors. Applying Algorithm 1 using the inaccurate AoAs degrades the performance. Thus, we next design a robust counterpart by formulating the design objective over the range of possible AoAs $\Theta(\theta, \epsilon)$, and seek to minimize the design objective for the worst-case scenario over this range. To that aim, we next detail the modification introduced to the signal recovery component of the design objective, after which we formulate the robust optimization problem and the algorithm we utilize to tackle it.

Signal Recovery: Our goal is to reformulate the recovery error of the desired signal \mathbf{s} from its estimate $\hat{\mathbf{s}}$ when the exact AoAs of the desired signals are unknown. For any quantized representation of $\hat{\mathbf{s}}$ and any estimate of the AoA vector θ , the decomposition (10) holds, and it is still true that only the latter term depends on the configuration of the analog pre-processing matrix \mathbf{A} . However, the former term in (10), which represents the MMSE, depends on the AoAs of the desired signals. Consequently, if there exists any uncertainty in the desired angles, one needs to characterize the non-decomposed

recovery error, $\mathbb{E}\{\|s - \hat{s}\|^2\}$, and can no longer consider only the distortion with respect to linear MMSE estimate \tilde{s} , $\mathbb{E}\{\|\tilde{s} - \hat{s}\|^2\}$, as the signal recovery performance measure.

We again let the digital processing output an estimate of the form $\hat{s} = \mathbf{B}\mathbf{Q}_b(\mathbf{A}\mathbf{x})$ for some $\mathbf{B} \in \mathbb{C}^{K \times P}$ and set the ADCs to have negligible overloading probability. By using the notations $\mathbf{C}_x(\boldsymbol{\theta})$ and $\mathbf{C}_{sx}(\boldsymbol{\theta})$ for covariance matrices in (4) to encapsulate their dependence on AoAs, we generalize the MSE expression in Lemma 1 as follows:

Lemma 2. *When the ADCs utilize non-subtractive dithered quantizers with vanishing overloading probability, then for any setting of the AoAs $\boldsymbol{\theta}$, the MSE objective (10) becomes*

$$\begin{aligned} \text{MSE}(\mathbf{A}, \mathbf{B}, \boldsymbol{\theta}) = & \text{Tr} \left(\mathbf{C}_s - 2\mathbf{C}_{sx}(\boldsymbol{\theta})\mathbf{A}^H\mathbf{B}^H \right. \\ & + \mathbf{B}\mathbf{A}\mathbf{C}_x(\boldsymbol{\theta})\mathbf{A}^H\mathbf{B}^H \\ & \left. + \mathbf{B} \frac{2\kappa \cdot \text{Tr}(\mathbf{A}\mathbf{C}_x(\boldsymbol{\theta})\mathbf{A}^H)}{3b^2 \cdot P} \mathbf{B}^H \right). \end{aligned} \quad (17)$$

Proof: See Appendix A. ■

For any fixed $\boldsymbol{\theta}$, it can be shown that the setting of \mathbf{B} which minimizes (17) is the one given in (12), for which the MSE expression in Lemma 2 coincides with the sum of the MMSE and the excess MSE of Lemma 1. However, since in the presence of uncertainty, we do not have exact knowledge of $\boldsymbol{\theta}$, but can only characterize a range in which it takes values, we cannot immediately substitute the MSE minimizing \mathbf{B} as we did in Section III, since each possible value of $\boldsymbol{\theta}$ is associated with a different MSE minimizing digital filter.

Similar to Lemma 1, Lemma 2 rigorously holds when ADCs are modeled as implementing non-subtractive dithered quantizers. For a broad range of input signals that do not satisfy this assumption, it also approximately holds.

Robust Optimization: Lemma 2 formulates the overall design objective for any possible $\boldsymbol{\theta}$. After adding the regularization terms to balance the contribution of interference rejection and the power consumption of the analog circuitry, the new design objective is formulated as

$$\mathcal{L}(\mathbf{A}, \mathbf{B}, \boldsymbol{\theta}) = \text{MSE}(\mathbf{A}, \mathbf{B}, \boldsymbol{\theta}) + \gamma_I \text{IntRej}(\mathbf{A}) + \gamma_S \|\mathbf{A}\|_{1,1}. \quad (18)$$

The robust optimization that minimizes the loss for the worst-case scenario is then given by

$$\mathbf{A}^\circ, \mathbf{B}^\circ = \arg \min_{\mathbf{A} \in \mathcal{A}^{P \times N}, \mathbf{B} \in \mathbb{C}^{K \times P}} \max_{\boldsymbol{\theta} \in \Theta(\boldsymbol{\theta}, \epsilon)} \mathcal{L}(\mathbf{A}, \mathbf{B}, \boldsymbol{\theta}). \quad (19)$$

Besides the fact that the optimization problem is formulated over the possibly non-convex search space \mathcal{A} , the objective in (19) is also not concave with respect to the variable $\boldsymbol{\theta}$. This makes the minimax optimization problem (19) difficult to solve. Yet, it can still be tackled with iterative solvers, even though they are not guaranteed to find the optimal solution.

Design Algorithm: A candidate approach to tackle (19) is to replace the order of minimization and maximization, i.e., convert it into a maximin problem, for which the internal minimization is carried out for a given $\boldsymbol{\theta}$, allowing to use the results of Section III. However, since we seek to minimize our objective, then by using the max-min inequality [45, Ch. 5.4],

such an approximation would result in minimizing a lower-bound on the objective (19), and thus does not necessarily yield a suitable design in the sense of the original minimax problem. Consequently, we directly tackle (19) numerically, replacing the continuous $\Theta(\boldsymbol{\theta}, \epsilon)$ with a set of C grid points $\{\boldsymbol{\theta}_c\}_{c=1}^C \subset \Theta(\boldsymbol{\theta}, \epsilon)$. We thus treat the surrogate problem

$$\begin{aligned} \mathbf{A}^\circ, \mathbf{B}^\circ = & \arg \min_{\mathbf{A} \in \mathcal{A}^{P \times N}, \mathbf{B} \in \mathbb{C}^{K \times P}} \min_{\gamma > 0} \gamma \\ & \text{subject to } \mathcal{L}(\mathbf{A}, \mathbf{B}, \boldsymbol{\theta}_c) \leq \gamma, \quad c \in \{1, \dots, C\}. \end{aligned} \quad (20)$$

The surrogate problem in (20) is convex with respect to both \mathbf{A} and \mathbf{B} , separately, when the analog combiner is unconstrained, i.e., $\mathcal{A} = \mathbb{C}$. Consequently, when $\mathcal{A} = \mathbb{C}$, (20) can be tackled using alternating optimization over both \mathbf{A} and \mathbf{B} . We convert the constrained (20) into an unconstrained optimization by formulating the logarithmic barrier function [46]

$$\begin{aligned} \mathcal{F}(\mathbf{A}, \gamma, \mathbf{B}) = & \gamma - \mu_h \sum_{c=1}^C \ln(\gamma - \text{MSE}(\mathbf{A}, \mathbf{B}, \boldsymbol{\theta}_c)) \\ & + \gamma_I \text{IntRej}(\mathbf{A}) + \gamma_S \|\mathbf{A}\|_{1,1}, \end{aligned} \quad (21)$$

where $\mu_h > 0$ is the barrier hyperparameter.

We next let $\bar{\mathcal{O}}_{\mathcal{F}_A}(\cdot)$ and $\bar{\mathcal{O}}_{\mathcal{F}_B}(\cdot)$ be iterative optimizers of (21) with respect to (\mathbf{A}, γ) and to (\mathbf{B}, γ) respectively. Similarly to the approach adopted in Subsection III-C, this can be achieved by defining the task term as $\tilde{\mathcal{F}}(\mathbf{A}, \gamma, \mathbf{B}) := \gamma - \mu_h \sum_{c=1}^C \ln(\gamma - \text{MSE}(\mathbf{A}, \mathbf{B}, \boldsymbol{\theta}_c)) + \gamma_I \text{IntRej}(\mathbf{A})$. We can now set $\bar{\mathcal{O}}_{\mathcal{F}_A}(\cdot)$ to be proximal gradient steps of the form

$$\bar{\mathcal{O}}_{\mathcal{F}_A}(\mathbf{A}, \gamma, \mathbf{B}) = \mathcal{T}_{\gamma_S} \left\{ (\mathbf{A}, \gamma) - \mu_A \nabla_{\mathbf{A}, \gamma} \tilde{\mathcal{F}}(\mathbf{A}, \gamma, \mathbf{B}) \right\}, \quad (22)$$

where \mathcal{T} denotes element-wise complex soft-thresholding (as in (15)). Similarly, $\bar{\mathcal{O}}_{\mathcal{F}_B}(\cdot)$ is a gradient step

$$\bar{\mathcal{O}}_{\mathcal{F}_B}(\mathbf{A}, \gamma, \mathbf{B}) = (\mathbf{B}, \gamma) - \mu_B \nabla_{\mathbf{B}, \gamma} \tilde{\mathcal{F}}(\mathbf{A}, \gamma, \mathbf{B}). \quad (23)$$

In (22)-(23), the hyperparameters μ_A, μ_B are the step-sizes. As in (15), the differentiability of $\tilde{\mathcal{F}}(\mathbf{A}, \gamma, \mathbf{B})$ allows computing its gradients using automatic differentiation tools.

The optimization for tackling (21) can be based on, e.g., alternating between a fixed number of iterations for setting \mathbf{A} using $\bar{\mathcal{O}}_{\mathcal{F}_A}(\cdot)$, followed by a fixed number of iterations for updating \mathbf{B} via $\bar{\mathcal{O}}_{\mathcal{F}_B}(\cdot)$, as we do in our numerical study in Section V. We follow the design strategy proposed in Subsection III-C, and augment its iterations with periodic projections onto the discrete set \mathcal{A} . To facilitate convergence to a suitable setting of \mathbf{A} and \mathbf{B} , we set their initial values to be the $\mathbf{A}^{(0)} = \mathbf{\Gamma}(\boldsymbol{\theta})$, and the digital filter $\mathbf{B}^{(0)}$ via (12). The resulting algorithm is summarized as Algorithm 2.

B. Hardware Non-Idealities

As shown in Fig. 3a, VMs are implemented with a quadrature all-pass filter and two variable gain amplifiers (VGAs). Quadrature all-pass filter generates the required I/Q components, while VGAs determine the set of complex phase/gain states that the VM can be configured to exhibit, i.e., the set \mathcal{A} . In the system described in Section III, the values in \mathcal{A} are assumed to be precisely known and can be ideally configured. However, when VMs are employed in practice, various

Algorithm 2: Robust Beamforming Design

Init: Set $\mathbf{A}^{(0)}, \mathbf{B}^{(0)}$

- 1 **for** $k = 1, 2, \dots, k_{\max}$ **do**
- 2 Set $\bar{\mathbf{A}}^{(0)} \leftarrow \mathbf{A}^{(k-1)}, \bar{\mathbf{B}}^{(0)} \leftarrow \mathbf{B}^{(k-1)}$;
- 3 Set $\gamma \leftarrow \max_c \mathcal{L}(\bar{\mathbf{A}}^{(0)}, \bar{\mathbf{B}}^{(0)}, \theta_c)$ via (18);
- 4 **for** $l = 1, 2, \dots, l_{\max}$ **do**
- 5 | Update $\bar{\mathbf{A}}^{(l)}, \gamma \leftarrow \bar{\mathcal{O}}_{\mathcal{F}_A}(\bar{\mathbf{A}}^{(l-1)}, \gamma, \mathbf{B}^{(k-1)})$;
- 6 **end**
- 7 Update $\mathbf{A}^{(k)} \leftarrow \bar{\mathbf{A}}^{(l_{\max})}$;
- 8 **if** $\text{mod}(k, k_{\text{proj}}) = 0$ **then**
- 9 | Project via $\mathbf{A}^{(k)} \leftarrow \mathcal{P}_{\mathcal{A}}(\mathbf{A}^{(k)})$
- 10 **end**
- 11 **for** $l = 1, 2, \dots, l_{\max}$ **do**
- 12 | Update $\bar{\mathbf{B}}^{(l)}, \gamma \leftarrow \bar{\mathcal{O}}_{\mathcal{F}_B}(\mathbf{A}^{(k)}, \gamma, \bar{\mathbf{B}}^{(l-1)})$;
- 13 **end**
- 14 Update $\mathbf{B}^{(k)} \leftarrow \bar{\mathbf{B}}^{(l_{\max})}$;
- 15 **end**

Output: Analog combiner $\mathbf{A}^{(k_{\max})}$ and digital processing matrix $\mathbf{B}^{(k_{\max})}$.

hardware non-idealities such as gain and phase mismatches at I/Q components or at the output of VM, make it impossible to realize the exact desired complex gains. These mismatches can be measured and are usually calibrated in the digital domain, which is less challenging than designing analog hardware with stricter design performance specifications. However, our need to operate low-resolution ADCs requires tightly coupled high-precision analog pre-processing and digital processing and necessitates calibrating the analog pre-processing. In the following, we integrate analog hardware calibration into our system design by incorporating phase and gain mismatches into the algorithm. To this end, we first propose a hardware-compliant model for the mismatches. The effect of mismatches is captured by scaling or rotation of the feasible mapping between VMs and the set \mathcal{A} .

Hardware Compliant Model: The mismatched hardware model is illustrated in Fig. 4. We denote gain and phase mismatches as $(\alpha_{p,n}, \beta_{p,n})$ and $(\zeta_{p,n}, \delta_{p,n})$ corresponding to the I/Q paths within the VM $[\mathbf{A}]_{p,n}$, respectively. Similarly, mismatches between different VMs stemming from routing delay and attenuation in practical hardware can be observed at the output paths of the VMs. Mismatches between different VMs are modeled at the output of Fig. 4 by letting $(\eta_{p,n}, \rho_{p,n})$ be gain and phase mismatch corresponding to the output path of the $[\mathbf{A}]_{p,n}$ entry, respectively. Under the mismatches in the VM corresponding to the $[\mathbf{A}]_{p,n}$ entry, the corrupted discrete set $\bar{\mathcal{A}}_{p,n}$, which the VM can realize, is given as:

$$\begin{aligned} \bar{\mathcal{A}}_{p,n} = & \left\{ (1 + \alpha_{p,n})(1 + \eta_{p,n})e^{j(\beta_{p,n} + \rho_{p,n})} \text{Re}\{a\} \right. \\ & \left. + (1 + \zeta_{p,n})(1 + \eta_{p,n})je^{j(\delta_{p,n} + \rho_{p,n})} \text{Im}\{a\} \mid a \in \mathcal{A} \right\}. \end{aligned} \quad (24)$$

To construct the corrupted set $\bar{\mathcal{A}}_{p,n}$, we need to measure the hardware mismatches. This is generally done by deactivating all except one VM and measuring the output. Hence, phase and gain mismatches are assumed known. The ideal case without any mismatch corresponds to $\alpha_{p,n} = \zeta_{p,n} = \eta_{p,n} = 0$ and $\beta_{p,n} = \delta_{p,n} = \rho_{p,n} = 0^\circ$ for all (p, n) , i.e. for every VM.

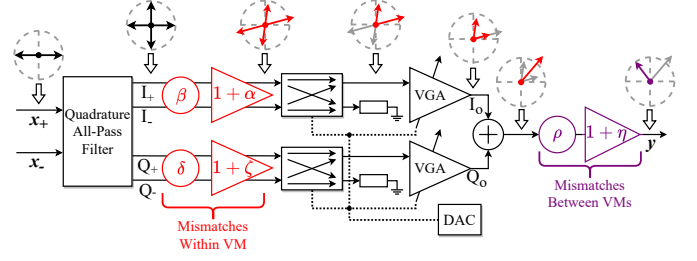


Fig. 4. VM architecture model with I/Q mismatches.

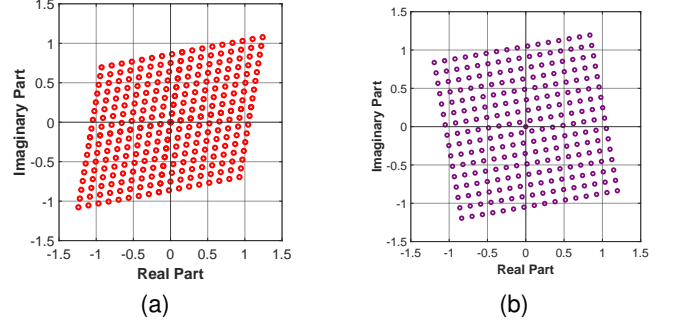


Fig. 5. 4-bit VM constellation under mismatches modeled by (24) (a) $(\alpha_{p,n}, \beta_{p,n}) = (-\zeta_{p,n}, -\delta_{p,n}) = (0.1, 10^\circ)$; (b) $(\eta_{p,n}, \rho_{p,n}) = (0.1, 10^\circ)$. Examples of mismatched normalized complex constellation diagrams are illustrated in Fig. 5.

Co-optimized Design: We next incorporate the proposed hardware-compliant model into our design, allowing it to cope with these mismatches. Compensating for hardware mismatches requires the knowledge of the gain and phase mismatches, which can be measured from the real hardware. After these mismatches are measured, we update the optimization problem in (14) to project onto the new set \mathcal{A}

$$\mathbf{A}^o = \arg \min_{[\mathbf{A}]_{p,n} \in \bar{\mathcal{A}}_{p,n}} \mathcal{L}(\mathbf{A}). \quad (25)$$

The optimization problem (25) has the same structure with (8), while having a different projection set. After defining the new projection set as $\bar{\mathcal{A}} = \{\mathbf{A} : [\mathbf{A}]_{p,n} \in \bar{\mathcal{A}}_{p,n}\}$, problem (25) is tackled by changing the projection step $\mathcal{P}_{\mathcal{A}}(\mathbf{A})$ with $\mathcal{P}_{\bar{\mathcal{A}}}(\mathbf{A})$ in Algorithm 1. While projection is still done element-wise, here $\mathcal{P}_{\bar{\mathcal{A}}}(\mathbf{A})$ cannot be obtained by separately quantizing the I/Q components, as in (16), and must be done directly, i.e.,

$$[\mathcal{P}_{\bar{\mathcal{A}}}(\mathbf{A})]_{p,n} = \arg \min_{a \in \bar{\mathcal{A}}} \|[\mathbf{A}]_{p,n} - a\|.$$

C. Discussion

Problem (19) represents the robust design as minimax optimization, in which the set over which maximization is carried out, $\Theta(\theta, \epsilon)$, is continuous. While there are minimax optimization algorithms designed to operate over continuous domains [47], for simplicity, we adopt a method geared towards finite maximization sets. In our numerical study, we observed that the performance of the system is not sensitive to the choice of the number of grid points, i.e. C .

The design of a robust system described in Subsection IV-A accounts for only the uncertainties in the AoAs of the desired

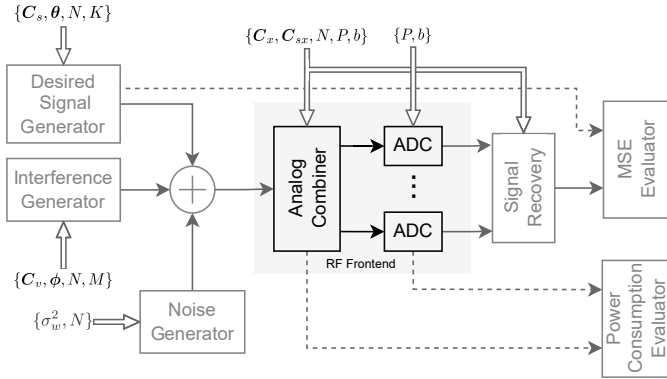


Fig. 6. Task-specific hybrid MIMO receiver system testbench.

signals. Nonetheless, one can follow the same algorithmic approach to make the system robust against other uncertainties such as the AoAs of interferers and power levels of the signals. This study is left for future research.

The design proposed in Subsection IV-B facilitates coping with hardware mismatches by measuring and incorporating them into the design procedure. Our algorithm relies on our proposed modeling of non-idealities such as amplitude-dependent phase shift in the VGAs [48]. Similarly, other VM implementations can give rise to different types of mismatches. Our design naturally extends to other forms of mismatches, as once the complex set \mathcal{A} and its mismatched counterpart $\tilde{\mathcal{A}}$ are correctly defined, it can be incorporated into Algorithms 1-2.

V. NUMERICAL EVALUATIONS

In this section, we evaluate the proposed hybrid MIMO receiver. We present the simulation setup in Subsection V-A. Next, in Section V-B, we characterize the MSE performance in signal recovery with and without mismatches and show robustness to mismatches. We demonstrate the system's ability to reject spatial interferers in Subsection V-C, and provide power consumption estimates in Subsection V-D.

A. Simulation Setup

To evaluate the task-agnostic MIMO receiver and estimate power savings, we utilize the simulation testbench illustrated in Fig. 6. The hardware system features an RF front end as an analog combiner and digital signal processing back end for signal recovery, as described in Subsection II-A. The N -element input \mathbf{x} is fed into the analog combiner \mathbf{A} at RF frequencies, down-converted to a low baseband frequency, and provided to the low-quantization rate ADCs as I/Q signals. In the digital domain, the filter \mathbf{B} is applied and signal recovery is performed. Recovery performance is characterized using MSE. Power savings of the system is evaluated over the total power consumption of the analog combiner and ADCs.

We simulate $K = 2$ desired signals at angles $\theta_1 = \frac{\pi}{8}, \theta_2 = -\frac{\pi}{4}$ with variances 1.5 and 0.5, respectively. We model $M = 2$ unwanted interferers at angles $\phi_1 = -\frac{\pi}{18}, \phi_2 = \frac{\pi}{3}$ with a variance of 5 for both sources. Consequently, the interferers are several times stronger than the desired signals. We define the signal-to-noise ratio (SNR) as the ratio between the average power level of desired signals to the power level of noise,

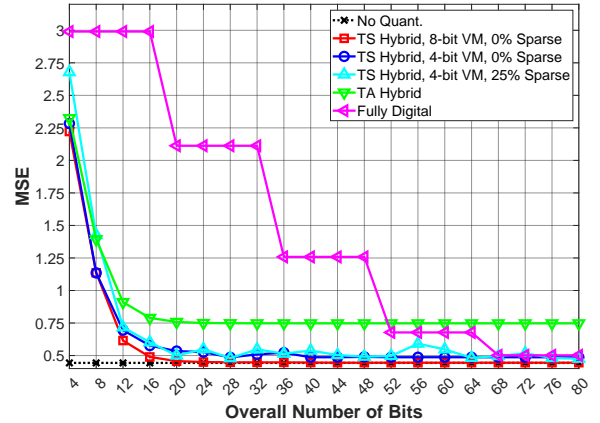


Fig. 7. MSE vs. the total number of quantization bits (SNR = 0 dB).

σ_w^2 . We consider a hybrid MIMO receiver with $N = 8$ half-wavelength spaced antenna elements and $P = 2$ RF chains, and $2 \cdot P = 4$ ADCs (*TS Hybrid*). For comparison purposes, we simulate a fully-digital MIMO receiver with infinite resolution quantization (*No Quant.*), whose MSE constitutes a lower bound on the achievable performance. We also simulate two MIMO receivers operating with quantization constraints: a fully-digital MIMO receiver (*Fully Digital*) and a task-agnostic hybrid MIMO system (*TA Hybrid*), where the analog combiner is tuned to beamform towards the AoAs θ .

B. MSE Performance

Non-mismatched Performance: We first evaluate the signal recovery MSE performance achieved using Algorithm 1 for various VM resolutions and sparsity levels of the analog matrix \mathbf{A} , without any non-idealities. The coefficients of the analog-combiner matrix \mathbf{A} are computed via Algorithm 1.

The MSE in recovering \mathbf{s} versus the overall number of bits, i.e., $2 \cdot P \lceil \log_2 b \rceil$, is depicted in Fig. 7. We show the numerical simulation results for 0% sparse operation with 8-bit VMs, and for 0% and 25% sparse \mathbf{A} with VMs quantized with relatively low resolution, e.g., 4-bit resolution. The SNR is set to 0 dB. We observe in Fig. 7 that by utilizing Algorithm 1, one can design a task-specific hybrid MIMO receiver using low-quantization rate ADCs to approach the MSE performance achieved without any quantization, while using low-resolution VMs, e.g., merely $2^4 = 16$ different settings for 4 bits, and deactivating 25% of VMs for sparsity to reduce power. The task-agnostic fully-digital MIMO receiver achieves substantially worse MSE at a comparable total ADC bit budget. For the same targeted MSE, more than $4 \times$ quantization rate reduction is observed with the proposed method. The conventional hybrid MIMO receiver, which only beamforms towards the desired angles, also demonstrates worse recovery MSE. Thus, the proposed method shows $1.5 \times$ lower MSE at the same quantization rate of 16 bits, as shown in Fig. 7.

The effect of the noise level on the recovery performance of the system is studied next. The MSE in recovering the desired signals versus the SNR is depicted in Fig. 8. The power level of the noise is swept whereas the power level of desired signals and interferences are unchanged to generate different

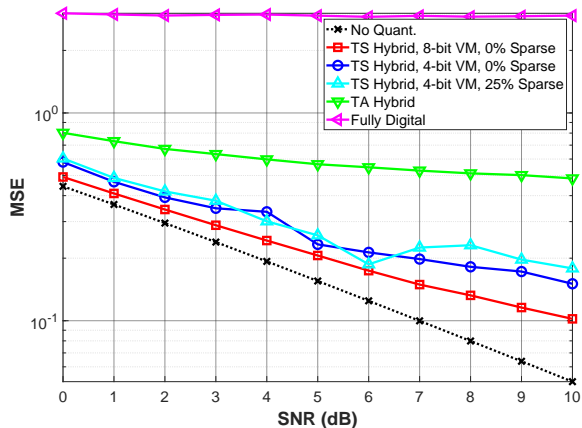


Fig. 8. MSE vs. SNR (Overall number of bits = 16).

SNRs ranging from 0dB to 10dB. The overall number of bits is 16, which is found to be a relatively low quantization rate where task-specific recovery via Algorithm 1 approaches to the MSE achieved without quantization. Here, the fully digital task-agnostic MIMO receiver achieves the highest MSE, and does not approach the performance floor at any SNR level. The conventional hybrid MIMO receiver achieves better MSE than the quantized fully-digital system, however, it is not able to deliver the same recovery MSE as the proposed algorithm. The MSE performance of the proposed method with different resolutions and sparsity levels achieves recovery performance close to the performance floor at every level of SNR, significantly outperforming the benchmark systems.

Performance under Inaccurate AoAs: We next study the recovery performance of the robust and non-robust designs when there exists an uncertainty in the AoAs. We evaluate recovery performance for 0% sparse \mathbf{A} with VMs quantized with 4-bit resolution. Error margin parameter ϵ is swept from 0° to 10° , and random AoA realizations within the interval $\Theta(\theta, \epsilon)$ are generated for each ϵ value. Subsequently, the MSE in the recovery of desired signals for all realizations is calculated for analog combiner \mathbf{A} which is configured by non-robust Algorithm 1 and robust Algorithm 2. We show the worst recovery MSE among all the AoA realizations. Finally, we evaluate the recovery MSE when the AoAs are accurate but the system is configured with the robust Algorithm 2.

The MSE in recovering s versus the error margin ϵ is depicted in Fig. 9. We set the SNR level to 0 dB and the overall number of bits to 16 bits. The system configured via the robust algorithm achieves better recovery performance for the worst-case scenario than a non-robust algorithm for all degrees of uncertainties. For error margins higher than 2° degrees, the robust system notably outperforms the non-robust system in terms of signal recovery. However, because of the fact that the robust algorithm minimizes the recovery error for the worst-case scenario over the range of possible angles, it is observed that if the system is configured with the robust algorithm even though the AoAs are accurate, worse MSE than the non-robust algorithm is obtained. Hence, one should use Algorithm 2 only if the AoAs are doubted to be accurate.

Next, we show how the MSE in recovering s is affected by

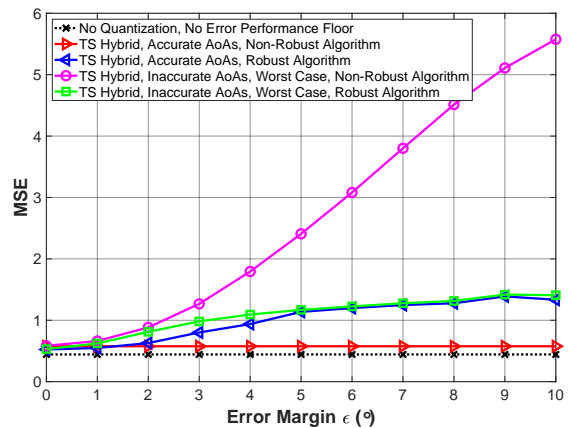


Fig. 9. MSE vs. error margin ϵ (SNR = 0 dB, overall number of bits = 16, TS Hybrid, 4-bit VM, 0% sparse).

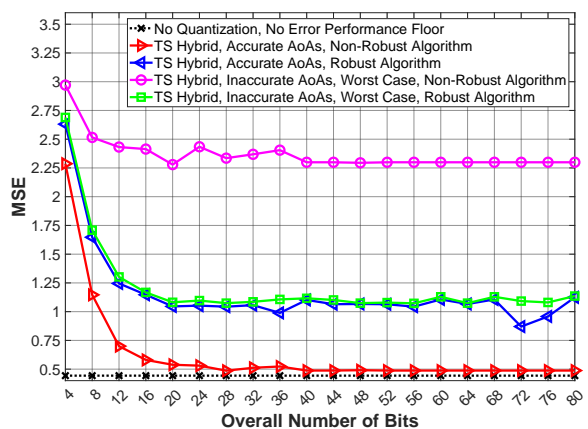


Fig. 10. MSE vs. overall number of bits (SNR = 0 dB, error margin $\epsilon = 5^\circ$, 4-bit VM, 0% sparse).

the overall number of bits when the AoAs are known up to some degree. We set the error margin to $\epsilon = 5^\circ$ and the SNR level to 0 dB. The results, reported in Fig. 10, demonstrate that the hybrid MIMO system configured via a non-robust Algorithm 1 receiver achieves worse recovery performance at a comparable total ADC bit budget. The proposed robust Algorithm 2 shows $2.1\times$ lower MSE than the non-robust Algorithm 1 at the quantization rate of ≥ 16 bits for the worst-case scenario in the possible range of AoAs. However, it shows $2.1\times$ higher MSE than non-robust Algorithm 1 at the same quantization rate of ≥ 16 bits when the AoAs are accurate.

Performance under Hardware Non-Idealities: We next consider the receiver operation under phase and gain mismatches in the VMs. The SNR and the overall number of bits are set to 0 dB and 16 bits, respectively. We evaluate the recovery performance for 25% sparse combiner with 4-bit VMs, comparing \mathbf{A} configured via Algorithm 1, which does not take into account the mismatches, and its co-optimized version that is described in Subsection IV-B. We present task-agnostic hybrid MIMO system performance under phase and gains mismatches as benchmarks, as well as show the system's performance without any mismatches. In practice, the total amount of such mismatches is random, but there are

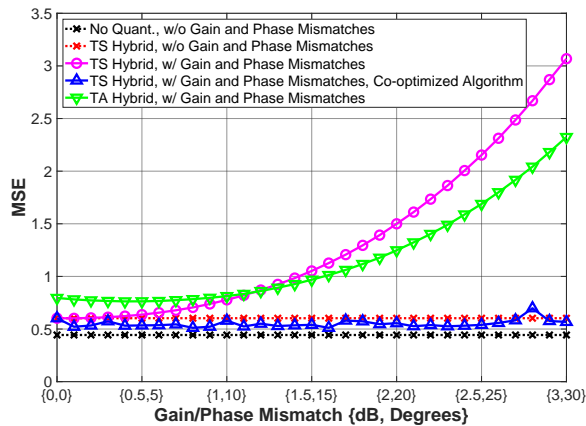


Fig. 11. MSE vs. gain and phase errors $(\alpha, \beta) = (-\zeta, -\delta) = (-2\eta, 2\rho)$ (SNR = 0 dB, overall number of bits = 16, 4-bit VM, 25% sparse).

fixed errors resulting from manufacturing processes and long-term aging effects. Consequently, in [29], [30], mismatches are modeled using random variables. Hence, to calculate the MSE in recovery under a practical scenario of gain and phase mismatches, we generate random realizations of phase and gain mismatch pairs, uniformly distributed around a given mean, with variations of $\pm 10\%$. In the co-optimized algorithm, we tune the analog combiner via the mean of the mismatches. The MSE performance of the system is evaluated by average recovery error among all realizations.

In numerical evaluations, we denote the mean of mismatch parameters as $(\alpha, \beta) \triangleq (\mathbb{E}\{\alpha_{p,n}\}, \mathbb{E}\{\beta_{p,n}\})$, $(\zeta, \delta) \triangleq (\mathbb{E}\{\zeta_{p,n}\}, \mathbb{E}\{\delta_{p,n}\})$ and $(\eta, \rho) \triangleq (\mathbb{E}\{\eta_{p,n}\}, \mathbb{E}\{\rho_{p,n}\})$ for every $n = \{1, 2, \dots, N\}$, $p = \{1, 2, \dots, P\}$ under the hardware-compliant model discussed in IV-B. The random mismatches are thus i.i.d. among all VMs. The MSE performance versus the mean gain and phase mismatches (α, β) is reported in Fig. 11, where we set mismatch pairs to be $(\alpha, \beta) = (-\zeta, -\delta) = (-2\eta, 2\rho)$. We observe in Fig. 11 that the proposed method clearly eliminates the MSE degradation due to hardware non-idealities. It is seen that for every mismatch level, the co-optimized algorithm achieves the performance of a non-mismatched hybrid MIMO system where mismatch unaware designs perform substantially worse in recovery.

C. Task-Specific Beamforming and Array Factors

Algorithm 1 designs the analog combiner to reject the spatial interferers in analog, in a joint manner with the main system task of recovering \mathbf{s} in digital. To evaluate and illustrate the desired suppression of interferers in analog, we next evaluate the receiver array factor (AF). The AF is a measure of a MIMO receiver gain as a function of an incoming signal's angular direction. An $N \times P$ MIMO receiver can generate P independent beams directed towards specific angles. The AF generated by \mathbf{A} at the p^{th} RF chain is computed as [13]

$$\text{AF}_p(\psi) = \sum_{n=1}^N [\mathbf{A}]_{p,n} e^{j\pi n \sin(\psi)}. \quad (26)$$

In addition to the setup described in Subsection V-A, we also consider another configuration with different angle realizations. The second setup consists of $K = 2$ desired signals

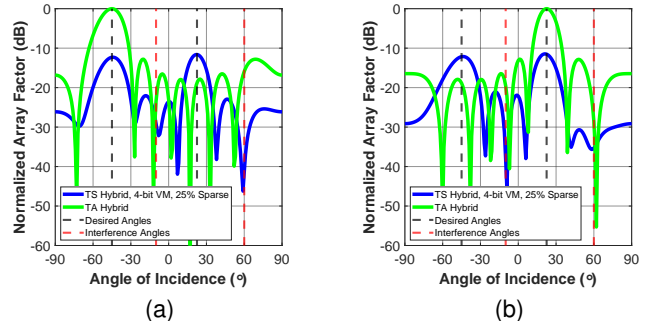


Fig. 12. AF for $P = 2$ where $K = 2$ desired signals at angles $\theta_1 = \pi/8$ $\theta_2 = -\pi/4$ and $M = 2$ interferers at angles $\phi_1 = -\pi/18$ $\phi_2 = \pi/3$ (SNR = 0 dB, overall 16 bits): (a) first output; (b) second output.

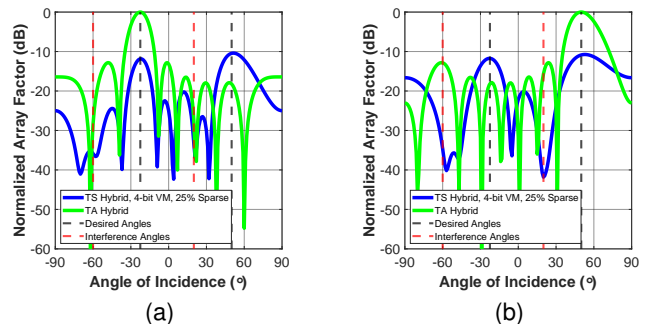


Fig. 13. AF for $P = 2$ where $K = 2$ desired signals at angles $\theta_1 = -\pi/8$ $\theta_2 = 5\pi/18$ and $M = 2$ interferers at angles $\phi_1 = -\pi/3$ $\phi_2 = \pi/9$ (SNR = 0 dB, overall 16 bits): (a) first output; (b) second output.

at angles $\theta_1 = -\frac{\pi}{8}$, $\theta_2 = \frac{5\pi}{18}$, and $M = 2$ interferers at angles $\phi_1 = -\frac{\pi}{3}$, $\phi_2 = \frac{\pi}{9}$, all having same variances as the first setup. The AF computed at the $P = 2$ analog outputs of the proposed system is illustrated in Fig. 12 and Fig. 13 where SNR level and the overall number of bits are set to 0 dB and 16 bits, respectively. It is compared with a task-agnostic conventional hybrid MIMO receiver whose analog combiner beamforms towards θ_1 (Fig. 12a-13a) and θ_2 (Fig. 12b-13b). The beam patterns achieved by Algorithm 1 are directed towards both the desired angles θ_1 and θ_2 , forming a linear combination of the desired signals at the output, while suppressing the interferers at angles ϕ_1, ϕ_2 by ≥ 36 dB. However, as observed in Fig. 12, since the analog combiner is not only optimized for beamforming but rather designed to facilitate recovery from quantized observations, our analog combiner achieves lower AF gain for the desired signals compared to the conventional beamforming. Nonetheless, the lower AF gain does not harm the task-specific recovery accuracy as shown in Fig. 7.

Next, we show the AF computed at the $P = 2$ analog outputs of the robust Algorithm 2 operating with inaccurate AoAs with error margin $\epsilon = 5^\circ$ in Fig. 14, and compare it with non-robust task-specific hybrid MIMO as well as task-agnostic conventional hybrid MIMO receiver. The robust analog combiner beamforms towards angles θ_1 (Fig. 14a) and θ_2 (Fig. 14b). It is observed that the peaks of the main lobes are flattened which enables better accuracy within the range possible AoAs while still being able to suppress the interferers at angles ϕ_1, ϕ_2 by ≥ 30 dB.

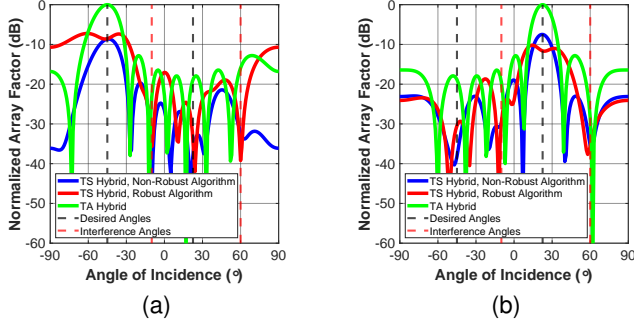


Fig. 14. AF for $P = 2$ where $K = 2$ desired signals at angles $\theta_1 = \pi/8$ $\theta_2 = -\pi/4$ and $M = 2$ interferers at angles $\phi_1 = -\pi/18$ $\phi_2 = \pi/3$ (SNR = 0 dB, overall 16 bits, error margin $\epsilon = 5^\circ$, 4-bit VM, 0% sparse): (a) first output; (b) second output.

D. Power Consumption Model

We conclude our numerical study by estimating the power consumption of the proposed hybrid MIMO receiver and the benchmark receivers. To that aim, we use the measured power consumption of hardware components reported in existing state-of-the-art integrated designs [10], [14], [33]–[37].

Accordingly, the power consumption of an $N \times N$ fully-digital MIMO receiver is estimated by:

$$P_{\text{FD}} = N \cdot P_{\text{LNA}} + N \cdot P_{\text{MIX}} + 2 \cdot N \cdot P_{\text{BB}} + 2 \cdot N \cdot P_{\text{ADC}}.$$

Here, P_{LNA} is the power consumed by a low-noise amplifier, P_{MIX} is the power of the mixer, and P_{BB} and P_{ADC} are baseband amplifier and ADC power consumption, respectively, doubled for I and Q paths.

The power consumed by an $N \times P$ hybrid MIMO receiver is estimated by:

$$P_{\text{HYB}} = \gamma_{SP} \cdot N \cdot P \cdot P_{\text{VM}} + P \cdot P_{\text{MIX}} + 2 \cdot P \cdot P_{\text{BB}} + 2 \cdot P \cdot P_{\text{ADC}}.$$

Here, P_{VM} is the power consumed by a low-noise VM-amplifier and γ_{SP} is the analog combiner sparsity coefficient: $\gamma_{SP} = 1$ denotes a non-sparse \mathbf{A} , while $\gamma_{SP} = 0.75$ corresponds to 25% sparsity.

The estimated power consumption of each hardware component and the total power consumption of task-specific and -agnostic MIMO receivers are summarized in Table I. The power scaling for various quantization levels of the VMs is based on [49] when using 8 bits for high-resolution VMs. For the ADC power estimation, we utilize Walden FoM [32], [37]. Our results show that the proposed power-saving techniques, e.g., 25% sparsity, 4-bit VMs, 4-bit ADCs, provide more than 58% reduction in power compared to the task-agnostic MIMO architectures using high-resolution ADCs, high-power LNAs, and high-resolution VMs. These notable power gains add to the improved MSE performance shown and the spatial interferer rejection observed in the previous subsections.

VI. CONCLUSION

In this work, we studied a power-efficient hybrid MIMO receiver design with embedded beamforming and low-resolution ADCs using task-specific quantization under certain practical non-idealities. We introduced a power-efficient analog and digital joint optimization framework, incorporating sparse analog

TABLE I
ESTIMATED POWER CONSUMPTION COMPARISON.

Hardware Component / System	Power (mW)
LNA/VM $P_{\text{LNA/VM}}$ (1-5 GHz 8 bit/4 bit) [14], [33]	20/10
Mixer with LO Gen (1-5 GHz) P_{MIX} [34], [35]	15
Baseband Amplifier P_{BB} [10]	5
ADC P_{ADC} (100 MS/s 10 bit/4 bit) [36], [50]	10/0.5
Fully-Digital MIMO Receiver (8×8)	520
Conventional Hybrid MIMO Receiver (8×2)	410
Task-Specific Hybrid MIMO Receiver (8×2)	172

combining and considering the finite resolution of the configurable analog hardware. Furthermore, we proposed a robust joint optimization algorithm to cope with mismatched AoAs, and extended our design to handle phase and gain errors. The proposed hybrid MIMO receiver notably outperforms the task-agnostic MIMO receivers by achieving improved MSE performance and successfully suppressing undesired spatial interferers at lower power and lower quantization rate, while being robust to common mismatches.

APPENDIX

A. Proof of Lemma 2

The MSE expression in (10) can be formulated as

$$\begin{aligned} \text{MSE} &= \mathbb{E}\{\|\mathbf{s} - \mathbf{B}\mathcal{Q}(\mathbf{A}\mathbf{x})\|^2\} \stackrel{(a)}{=} \mathbb{E}\{\|\mathbf{s} - \mathbf{B}(\mathbf{A}\mathbf{x} + \mathbf{e})\|^2\} \\ &\stackrel{(b)}{=} \mathbb{E}\{\|\mathbf{s} - \mathbf{B}(\mathbf{A}\mathbf{x})\|^2\} + \mathbb{E}\{\|\mathbf{B}\mathbf{e}\|^2\}. \end{aligned} \quad (27)$$

Here, (a) follows from [51, Thm. 2] when $\Pr(|(\mathbf{A}\mathbf{x}_l + d_l)| > \gamma) = 0$, where γ is the dynamic range of ADCs and d_l is the dither signal. Namely, the sum of the input to the ADCs and dither signal is always within the dynamic range, thus the output of the ADCs can be written as $\mathbf{A}\mathbf{x} + \mathbf{e}$ where \mathbf{e} is the quantization noise. Furthermore, by [21, Thm. 1], \mathbf{e} is uncorrelated with observation \mathbf{x} , and the desired signal \mathbf{s} , i.e., $\mathbb{E}\{\mathbf{x}\mathbf{e}^H\} = 0$ and $\mathbb{E}\{\mathbf{s}\mathbf{e}^H\} = 0$, which implies (b), and has uncorrelated zero-mean entries with variance $\frac{\Delta_p^2}{6}$, where $\Delta_p = \frac{2\gamma}{b}$ is the quantization spacing.

By distributing each term and using the linearity and cyclic property of the trace operator we have $\text{MSE} = \text{Tr}\left(\mathbf{C}_s - 2\mathbf{C}_{s\mathbf{x}}\mathbf{A}^H\mathbf{B}^H + \mathbf{B}\mathbf{A}\mathbf{C}_x\mathbf{A}^H\mathbf{B}^H + \mathbf{B}\frac{\Delta_p^2}{6}\mathbf{B}^H\right)$. Finally, setting $\kappa := \eta^2(1 - \frac{\eta^2}{3b^2})^{-1}$ where η is a coefficient tuned to guarantee negligible overloading probability of the ADCs, and adapting [21, Thm. 1], yields

$$\begin{aligned} \text{MSE} &= \text{Tr}\left(\mathbf{C}_s - 2\mathbf{C}_{s\mathbf{x}}\mathbf{A}^H\mathbf{B}^H \right. \\ &\quad \left. + \mathbf{B}\mathbf{A}\mathbf{C}_x\mathbf{A}^H\mathbf{B}^H + \mathbf{B}\frac{2\kappa \cdot \text{Tr}(\mathbf{A}\mathbf{C}_x\mathbf{A}^H)}{3b^2 \cdot P}\mathbf{B}^H\right), \end{aligned}$$

thus proving the lemma.

REFERENCES

- [1] T. Zirtoglu, N. Shlezinger, Y. C. Eldar, and R. T. Yazicigil, “Power-efficient hybrid MIMO receiver with task-specific beamforming using low-resolution ADCs,” in *Proc. IEEE ICASSP*, 2022, pp. 5338–5342.
- [2] V. Wong, R. Schober, D. Ng, and L. Wang, *Key Technologies for 5G Wireless Systems*. Cambridge University Press, 2017.

- [3] M. Agiwal, A. Roy, and N. Saxena, "Next generation 5G wireless networks: A comprehensive survey," *IEEE Commun. Surveys Tuts.*, vol. 18, no. 3, pp. 1617–1655, 2016.
- [4] N. Shlezinger and Y. C. Eldar, "On the spectral efficiency of noncooperative uplink massive MIMO systems," *IEEE Trans. Commun.*, vol. 67, no. 3, pp. 1956–1971, 2018.
- [5] D. Gesbert, M. Shafi, D. shan Shiu, P. Smith, and A. Naguib, "From theory to practice: an overview of MIMO space-time coded wireless systems," *IEEE J. Sel. Areas Commun.*, vol. 21, pp. 281–302, 2003.
- [6] F. Rusek, D. Persson, B. K. Lau, E. G. Larsson, T. L. Marzetta, O. Edfors, and F. Tufvesson, "Scaling up MIMO: Opportunities and challenges with very large arrays," *IEEE Signal Process. Mag.*, vol. 30, no. 1, pp. 40–60, 2013.
- [7] N. Shlezinger, Y. C. Eldar, and M. R. Rodrigues, "Asymptotic task-based quantization with application to massive MIMO," *IEEE Trans. Signal Process.*, vol. 67, no. 15, pp. 3995–4012, 2019.
- [8] Y. C. Eldar, *Sampling Theory: Beyond Bandlimited Systems*. Cambridge University Press, 2015.
- [9] R. Walden, "Analog-to-digital converter survey and analysis," *IEEE J. Sel. Areas Commun.*, vol. 17, no. 4, pp. 539–550, 1999.
- [10] R. Méndez-Rial, C. Rusu, N. González-Prelcic, A. Alkhateeb, and R. W. Heath, "Hybrid MIMO architectures for millimeter wave communications: Phase shifters or switches?" *IEEE Access*, vol. 4, pp. 247–267, 2016.
- [11] S. S. Ioushua and Y. C. Eldar, "A family of hybrid analog-digital beamforming methods for massive MIMO systems," *IEEE Trans. Signal Process.*, vol. 67, no. 12, pp. 3243–3257, 2019.
- [12] C. Huang, S. Hu, G. C. Alexandropoulos, A. Zappone, C. Yuen, R. Zhang, M. Di Renzo, and M. Debbah, "Holographic MIMO surfaces for 6G wireless networks: Opportunities, challenges, and trends," *IEEE Wireless Commun.*, vol. 27, no. 5, pp. 118–125, 2020.
- [13] M. C. M. Soer, E. A. M. Klumperink, B. Nauta, and F. E. van Vliet, "Spatial interferer rejection in a four-element beamforming receiver front-end with a switched-capacitor vector modulator," *IEEE J. Solid-State Circuits*, vol. 46, no. 12, pp. 2933–2942, 2011.
- [14] M. C. M. Soer, E. A. M. Klumperink, D.-J. van den Broek, B. Nauta, and F. E. van Vliet, "Beamformer with constant-gm vector modulators and its spatial intermodulation distortion," *IEEE J. Solid-State Circuits*, vol. 52, no. 3, pp. 735–746, 2017.
- [15] H. Krishnaswamy and L. Zhang, "Analog and RF interference mitigation for integrated MIMO receiver arrays," *Proc. IEEE*, vol. 104, no. 3, pp. 561–575, 2016.
- [16] S. Golabighezalahmad, E. A. Klumperink, and B. Nauta, "A 0.7-5.7 GHz reconfigurable MIMO receiver architecture for analog spatial notch filtering using orthogonal beamforming," *IEEE J. Solid-State Circuits*, vol. 56, no. 5, pp. 1527–1540, 2020.
- [17] J. Mo, A. Alkhateeb, S. Abu-Surra, and R. W. Heath, "Hybrid architectures with few-bit ADC receivers: Achievable rates and energy-rate tradeoffs," *IEEE Trans. Wireless Commun.*, vol. 16, no. 4, pp. 2274–2287, 2017.
- [18] K. Roth, H. Pirzadeh, A. L. Swindlehurst, and J. A. Nossek, "A comparison of hybrid beamforming and digital beamforming with low-resolution ADCs for multiple users and imperfect CSI," *IEEE J. Sel. Topics Signal Process.*, vol. 12, no. 3, pp. 484–498, 2018.
- [19] J. Choi, J. Sung, B. L. Evans, and A. Gatherer, "Antenna selection for large-scale MIMO systems with low-resolution ADCs," in *Proc. IEEE ICASSP*, 2018, pp. 3594–3598.
- [20] Y. Li, C. Tao, G. Seco-Granados, A. Mezghani, A. L. Swindlehurst, and L. Liu, "Channel estimation and performance analysis of one-bit massive MIMO systems," *IEEE Trans. Signal Process.*, vol. 65, no. 15, pp. 4075–4089, 2017.
- [21] N. Shlezinger, Y. C. Eldar, and M. R. Rodrigues, "Hardware-limited task-based quantization," *IEEE Trans. Signal Process.*, vol. 67, no. 20, pp. 5223–5238, 2019.
- [22] P. Neuhaus, N. Shlezinger, M. Dörpinghaus, Y. C. Eldar, and G. Fettweis, "Task-based analog-to-digital converters," *IEEE Trans. Signal Process.*, vol. 69, pp. 5403–5418, 2021.
- [23] N. Shlezinger and Y. C. Eldar, "Deep task-based quantization," *Entropy*, vol. 23, no. 1, p. 104, 2021.
- [24] S. Salamatian, N. Shlezinger, Y. C. Eldar, and M. Médard, "Task-based quantization for recovering quadratic functions using principal inertia components," in *Proc. IEEE ISIT*, 2019, pp. 390–394.
- [25] H. Wang, N. Shlezinger, Y. C. Eldar, S. Jin, M. F. Imani, I. Yoo, and D. R. Smith, "Dynamic metasurface antennas for MIMO-OFDM receivers with bit-limited ADCs," *IEEE Trans. Commun.*, vol. 69, no. 4, pp. 2643–2659, 2021.
- [26] N. Shlezinger, R. J. G. van Sloun, I. A. M. Huijben, G. Tsintsadze, and Y. C. Eldar, "Learning task-based analog-to-digital conversion for MIMO receivers," in *Proc. IEEE ICASSP*, 2020, pp. 9125–9129.
- [27] F. Xi, N. Shlezinger, and Y. C. Eldar, "BiLiMO: Bit-limited MIMO radar via task-based quantization," *IEEE Trans. Signal Process.*, vol. 69, pp. 6267–6282, 2021.
- [28] X. Zhang, Z. He, B. Liao, X. Zhang, and W. Peng, "Robust quasi-adaptive beamforming against direction-of-arrival mismatch," *IEEE Trans. Aerosp. Electron. Syst.*, vol. 54, no. 3, pp. 1197–1207, 2018.
- [29] D. Mishra and H. Johansson, "Efficacy of hybrid energy beamforming with phase shifter impairments and channel estimation errors," *IEEE Signal Process. Lett.*, vol. 26, no. 1, pp. 99–103, 2019.
- [30] O. M. Bakr and M. Johnson, "Impact of phase and amplitude errors on array performance," EECS Department, University of California, Berkeley, Tech. Rep. UCB/EECS-2009-1, Jan 2009.
- [31] F. Ellinger, U. Mayer, M. Wickert, N. Joram, J. Wagner, R. Eickhoff, I. Santamaria, C. Scheytt, and R. Kraemer, "Integrated adjustable phase shifters," *IEEE Microw. Mag.*, vol. 11, no. 6, pp. 97–108, 2010.
- [32] P. Skrimponis *et al.*, "Power consumption analysis for mobile mmWave and sub-THz receivers," in *6G Wireless Summit*, 2020.
- [33] N. Joram, U. Mayer, R. Eickhoff, and F. Ellinger, "Fully integrated active CMOS vector modulator for 802.11a compliant diversity transceivers," in *IEEE International Conference on Microwaves, Communications, Antennas and Electronics Systems*, 2009.
- [34] A. Amer, E. Hegazi, and H. F. Ragaie, "A 90-nm wideband merged cmos lna and mixer exploiting noise cancellation," *IEEE J. Solid-State Circuits*, vol. 42, no. 2, pp. 323–328, 2007.
- [35] K. Kibaroglu and G. M. Rebeiz, "A 0.05–6 GHz voltage-mode harmonic rejection mixer with up to 30 dBm in-band IIP3 and 35 dBc HRR in 32 nm SOI CMOS," in *IEEE RFIC*, 2017, pp. 304–307.
- [36] C.-C. Ho and T.-C. Lee, "A 10-bit 200-MS/s reconfigurable pipelined A/D converter," in *Proceedings of Technical Program of 2012 VLSI Design, Automation and Test*, 2012.
- [37] H.-S. Lee and C. G. Sodini, "Analog-to-digital converters: Digitizing the analog world," *Proc. IEEE*, vol. 96, no. 2, pp. 323–334, 2008.
- [38] N. Joram, U. Mayer, R. Eickhoff, and F. Ellinger, "Fully integrated active cmos vector modulator for 802.11a compliant diversity transceivers," in *IEEE International Conference on Microwaves, Communications, Antennas and Electronics Systems*, 2009.
- [39] K.-J. Koh and G. M. Rebeiz, "0.13- μm CMOS phase shifters for X-, Ku-, and K-band phased arrays," *IEEE J. Solid-State Circuits*, vol. 42, no. 11, pp. 2535–2546, 2007.
- [40] R. T. Yazicigil, T. Haque, M. R. Whalen, J. Yuan, J. Wright, and P. R. Kinget, "Wideband rapid interferer detector exploiting compressed sampling with a quadrature analog-to-information converter," *IEEE J. Solid-State Circuits*, vol. 50, no. 12, pp. 3047–3064, 2015.
- [41] S. Foucart and H. Rauhut, *A mathematical introduction to compressive sensing*. Springer, 2013.
- [42] D. Maclaurin, D. Duvenaud, and R. P. Adams, "Autograd: Effortless gradients in numpy," in *ICML*, vol. 238, no. 5, 2015.
- [43] V. Monga, Y. Li, and Y. C. Eldar, "Algorithm unrolling: Interpretable, efficient deep learning for signal and image processing," *IEEE Signal Process. Mag.*, vol. 38, no. 2, pp. 18–44, 2021.
- [44] N. Shlezinger, Y. C. Eldar, and S. P. Boyd, "Model-based deep learning: On the intersection of deep learning and optimization," *IEEE Access*, vol. 10, pp. 115 384–115 398, 2022.
- [45] S. P. Boyd and L. Vandenberghe, *Convex optimization*. Cambridge University Press, 2004.
- [46] R. A. Waltz, J. L. Morales, J. Nocedal, and D. Orban, "An interior algorithm for nonlinear optimization that combines line search and trust region steps," *Mathematical Programming*, vol. 107, pp. 391–408, 2006.
- [47] K. K. Thekumparampil, P. Jain, P. Netrapalli, and S. Oh, "Efficient algorithms for smooth minimax optimization," *Advances in Neural Information Processing Systems*, vol. 32, 2019.
- [48] U. Mayer, M. Wickert, R. Eickhoff, and F. Ellinger, "Multiband mixed-signal vector modulator IC," in *IEEE RFIC*, 2011.
- [49] H. J. Qian, B. Zhang, and X. Luo, "High-resolution wideband phase shifter with current limited vector-sum," *IEEE Trans. Circuits Syst. I*, vol. 66, no. 2, pp. 820–833, 2019.
- [50] B. Ginsburg and A. Chandrakasan, "A 500MS/s 5b ADC in 65nm CMOS," in *2006 Symposium on VLSI Circuits, 2006. Digest of Technical Papers.*, 2006, pp. 140–141.
- [51] R. Gray and T. Stockham, "Dithered quantizers," *IEEE Trans. Inf. Theory*, vol. 39, no. 3, pp. 805–812, 1993.